Effect of geometry on magnetism of Hund's metals: Case study of BaRuO₃

Hrishit Banerjee [1,2] Hermann Schnait [2] Markus Aichhorn,[2] and Tanusri Saha-Dasgupta [3,*]

[1]*Yusuf Hamied Department of Chemistry, University of Cambridge, Lensfield Road, CB2 1EW, Cambridge, United Kingdom*

[2]*Institute of Theoretical and Computational Physics, Graz University of Technology, NAWI Graz, Petersgaße 16, Graz 8010, Austria*

[3]*Department of Condensed Matter Physics and Materials Science, S. N. Bose National Centre for Basic Sciences, Block JD, Sector-III, Salt lake, Kolkata-700106, India*

In order to explore the effects of structural geometry on the properties of correlated metals we investigate the magnetic properties of cubic (3C) and hexagonal (4H) BaRuO₃. While the 3C variant of BaRuO₃ is ferromagnetic below 60 K, the 4H phase does not show any long-range magnetic order, though, there is experimental evidence of short-range antiferromagnetic correlations. Employing a combination of computational tools, namely, density-functional theory and dynamical mean-field theory calculations, we probe the origin of contrasting magnetic properties of BaRuO₃ in the 3C and 4H structures. Our study reveals that the difference in connectivity of RuO₆ octahedra in the two phases results in different Ru-O covalency, which in turn influences substantially the strengths of screened interaction values for Hubbard U and Hund's rule J. With estimated U and J values, the 3C phase turns out to be a ferromagnetic metal, while the 4H phase shows paramagnetic behavior with vanishing ordered moments. However, this paramagnetic phase bears signatures of antiferromagnetic correlations, as confirmed by a calculation of the magnetic susceptibility. We find that the 4H phase is found to be at the verge of antiferromagnetic long-range order, which can be stabilized upon slight changes of screened Coulomb parameters U and J, opening up the possibility of achieving a rare example of an antiferromagnetic metal.

I. INTRODUCTION

Transition metal oxides (TMOs) represent a class of compounds exhibiting a plethora of fascinating physical properties [1]. For instance, the intriguing interplay of charge, spin, and orbital degrees of freedom in the context of strong correlations opens up a scientifically rewarding playground. While most studies focus on the interplay of charge, spin, and orbitals, the effect of geometry of the underlying structure is comparably less explored. This is, however, an equally important issue, given the fact that keeping the basic motif of transition metal oxygen octahedra, the connectivity of these octahedra in transition metal oxides can greatly vary from compound to compound.

To explore the influence of variation of connectivity in a systematic manner, it is desirable to find a structural variation within the same chemical composition in systems, where the interplay of geometry and correlation effect is expected to be strong. Moving down the periodic table from the 3d to the 4d transition metal series, the covalency between transition metal and oxygen increases. This leads to a large crystal field splitting between e_g and t_{2g} states that is usually of the order of the local screened Coulomb interaction U. Furthermore, the larger spatial extent of the 4d orbitals produces a larger band width as compared to 3d materials. As a result, the 4d compounds prefer a low-spin state rather than the high-spin state, with occupied t_{2g} and empty e_g configurations. While

4d compounds generally show a smaller screened Coulomb interaction U as compared to 3d compounds, the multiorbital nature of the problem in the t_{2g} manifold makes the Hund's coupling J an important parameter [2]. From that perspective, the interplay between the structural aspects and the electronic correlations driven by U and J in 4d TMOs may turn out to be more interesting than that for their 3d counterparts.

Ruthenates are an ideal playground for studying the 4d physics described above. A large number of ruthenate compounds have been experimentally synthesized, and a number of interesting physical phenomena has been reported, most of them being a manifestation of correlation effects. To mention a few, Sr₂RuO₄ is known for its unconventional p-wave superconductivity [3]. The properties of SrRuO₃ are reported to exhibit sensitivity to strain and compression, e.g., change in Curie temperature under compression and change in longitudinal resistivity and magnetic anisotropy to differential methods of strain application [4], while BaRu₆O₁₂ shows a quantum phase transition in transport and magnetic properties. Although the strong correlation effect in the 214 family is established, the large mass renormalization as found in photoemission [5] as well as the presence of incoherent features in optical conductivity [6], hints towards the importance of correlation effect in the 113 family too.

Among the ruthenate TMOs, BaRuO₃ (BRO), which is the sister compound of the well-studied compounds SrRuO₃ and CaRuO₃, offers a perfect platform for the exploration of the above-mentioned geometry effects in a systematic manner. Both SrRuO₃ and BRO, which are isoelectronic ruthenates

*t.sahadasgupta@gmail.com

(Ru^{4+} with $4d^4$ electronic configuration), have been considered as prototypical examples of Hund's metals with nearly spin-frozen states [7,8]. However, BRO is reported to exhibit structural and physical properties different from SrRuO$_3$ or CaRuO$_3$. The presence of Ba^{2+} at the A site, which has a larger ionic size compared to Sr^{2+} or Ca^{2+}, leads to a tolerance factor of BRO of $t = \frac{(r_{Ba}+r_O)}{\sqrt{2}(r_{Ru}+r_O)} > 1$ (where r_{Ba}, r_{Ru}, and r_O correspond to the radius of Ba, Ru, and O ions, respectively), favoring the hexagonal polytype as opposed to SrRuO$_3$ or CaRuO$_3$, for which $t < 1$ favors an orthorhombic structure with cubic stacking. Depending on the synthesis pressure, a sequence of structural types in BRO is reported from $9R$ (ambient pressure) to $4H$ (3 GPa) to $6H$ (5 GPa), all based on hexagonal symmetry [9]. Interestingly enough, the cubic $3C$ phase of BRO could also be stabilized under very high pressure conditions [10], giving rise to the unique opportunity of studying the influence of hexagonal versus cubic connectivity of RuO$_6$ octahedra within the same chemical formula of BRO. The four structures, synthesized under different pressure conditions, can be stabilized down to ambient pressure [9,10].

While $3C$ has only corner-shared connectivity, $4H$ has a combination of face-shared and corner-shared connectivity. The $6C$ and $9R$ structures also contain combinations of face-shared and corner-shared connectivity. The percentage of corner-shared connectivity is 50% for $4H$; it is 33% and 66% for the $9R$ and $6H$ phases, respectively. The structures of $6H$ and $9R$ are, however, much more complex. In $9R$ three RuO$_6$ octahedra share faces with each other, giving rise to a Ru$_3$O$_{12}$ trioctahedron unit which connects to another trioctahedron unit through the corner sharing, while for $6H$ the Ru$_2$O$_9$ dioctahedron unit and single RuO$_6$ octahedral unit arrange alternately and connect to each other through the connecting oxygen. However, the magnetic properties of more complex $9R$ and $6H$ are similar to that of $4H$. Both $4H$ and $6H$ are paramagnetic metals. The low-temperature conducting properties of $9R$, though, are debated, showing an upturn in resistivity in otherwise metallic conductivity. Phenomena like formation of charge density wave have been suggested for it [11]. To make the situation computationally tractable, we thus take up the $3C$ and $4H$ phase of BRO as a case study to investigate the effect of geometry on correlation-driven magnetism and the electronic structure of $4d$ TMOs. Cubic BRO with perovskite structure and corner-shared RuO$_6$ octahedra is a ferromagnetic metal, with a $T_c \sim 60$ K [10]. On the other hand, the moderate-pressure $4H$ phase, which exhibits nonperovskite hexagonal geometry with face-shared dimers of RuO$_6$ octahedra does not seem to order magnetically in experimental studies, although some signatures of antiferromagnetic correlations have been reported [5], suggesting a paramagnetic metal as a ground state [9]. The change in geometry from cubic to hexagonal, thus, appears to have a profound effect on the material's properties. We investigate this issue by a combination of a variety of tools, ranging from first-principles density-functional theory calculations to constrained random-phase approximation and dynamical mean-field theory. For the latter, we employ both a continuous-time quantum Monte Carlo technique using the hybridization expansion, as well as the fork tensor product

states method. Our study reveals a Hund's metallic state for both $3C$ and $4H$ phases, reflected in a strong dependence of the imaginary part of the self-energies upon variation of Hund's coupling. For small coupling, the imaginary parts at zero frequency, i.e., the electron-electron scattering rates, are small, and they increase to large values for increasing Hund's coupling. This emphasizes the importance of correlation effects for the description of the properties of BRO in both $3C$ and $4H$ phases. Ferromagnetically ordered phases, short-range antiferromagnetic fluctuations, and long-range ordered antiferromagnetic phases are found for both $3C$ and $4H$ in parameter space of Coulomb correlation U and Hund's coupling J. The central finding of our study is that the change in connectivity between $3C$ and $4H$ results in a change in metal-oxygen hybridization which influences the electronic screening, amounting to distinctly different estimated values of U and J for $3C$ and $4H$, respectively. This difference in the parameters places the $3C$ phase in the ferromagnetically ordered regime, and $4H$ in the paramagnetic regime with short-range antiferromagnetic correlations. It is intriguing to note that a slight variation of the U parameter would stabilize a rare and exotic example of an antiferromagnetically ordered metallic phase in the $4H$ variant, which could be used in spintronics applications.

II. COMPUTATIONAL DETAILS

Our density-functional theory (DFT) calculations for structural relaxation were carried out in a plane-wave basis with projector-augmented wave potentials [12] as implemented in the Vienna *Ab initio* Simulation Package (VASP) [13,14]. For ionic relaxations using the VASP package, internal positions of the atoms were allowed to relax until the forces became less than 0.005 eV/Å. For $3C$ there is no internal coordinate to be optimized, since all atoms are located in high-symmetry positions. For $4H$, the comparison of the oxygen positions between experimental and the nonmagnetic DFT relaxed structure show the changes to be negligible. An energy cutoff of 550 eV, and a $6 \times 6 \times 4$ Monkhorst-Pack k-points mesh provided good convergence of the total energy. Our *ab initio* dynamical mean-field theory (DMFT) calculations are based on the full-potential augmented plane-wave basis as implemented in WIEN2K [15]. For these calculations, we used the largest possible muffin-tin radii, and the basis set plane-wave cutoff as defined by $R_{min}K_{max} = 7.5$, where R_{min} is the muffin-tin radius of the oxygen atoms. In all our DFT calculations, we chose as exchange-correlation functional the generalized gradient approximation (GGA), implemented following the Perdew-Burke-Ernzerhof prescription [16]. The consistency between VASP and WIEN2K results have been cross-checked.

To facilitate a direct comparison between $3C$ and $4H$, and to keep the same unit cell for magnetic and nonmagnetic cases, a $\sqrt{2} \times \sqrt{2} \times 2$ supercell of $3C$ cubic phase primitive cell was considered. This created four Ru atoms in the unit cell of both $4H$ and $3C$.

We also perform constrained random phase approximation (cRPA) calculations within VASP, with the states of interest derived from a WANNIER90 projection method [17], to

have an estimate of the Hubbard U and Hund's J values for both geometries. This involves a three-step procedure: a DFT ground-state calculation, a calculation to obtain a number of virtual orbitals, and the actual cRPA calculation. For the Wannier projections an energy window from -2.5 to $+2$ eV around the Fermi energy was chosen, and projections were done to the t_{2g} states. A large number of bands (96 bands) were taken into account for the $G0W0$ calculation. The screened Hubbard U and Hund's J are obtained from the calculation as the static $\omega = 0$ limit of the frequency-dependent cRPA interactions. To cross-check the estimated U and J from cRPA, we have performed additional calculations of the Hubbard parameters using the linear response density-functional perturbation theory (DFPT) method implemented in the Hubbard parameters (HP) package of QUANTUM ESPRESSO [18–21].

We perform the DMFT calculations in a basis set of maximally localized Wannier functions (MLWFs) using WANNIER90 and the WIEN2WANNIER [22] interface. DMFT calculations were performed using the TRIQS/DFTTOOLS package [23–25] based on the TRIQS libraries [26]. Projective Wannier functions as implemented in the dmftproj module of TRIQS were employed to cross-check the results and also to calculate the initial occupancy of the correlated orbitals. The DMFT calculations in both MLWF and projective Wannier functions basis have been found to yield consistent results. In both cases a projection window of -2.5 to $+2$ eV was chosen.

For both paramagnetic and magnetic calculations, only Ru t_{2g} orbitals have been considered for the DMFT calculation. Low-energy models consisting of only t_{2g} orbitals have been extensively and very successfully used, and found to be adequate in many past works on ruthenates [7,8,27,28]. The e_g orbitals are higher in energy and are, thus, mostly empty. Calculation of the e_g occupancy in $3C$ BRO using dmftproj in this energy range yields occupations of only $0.02e^-$ for each orbital, which is negligible as compared to the t_{2g} occupation. Nevertheless, in order to cross-check our results, we have explicitly included the influence of the e_g by performing a set of calculations in the full d manifold. Our additional calculations establish that the model including all five d orbitals leads to essentially the same results as the t_{2g}-only model for the difference between $3C$ and $4H$ within the parameter regions of interest.

The Ru t_{2g} states hybridize with O p. One possible way to handle this situation is to explicitly take the oxygen states into account and construct a so-called d-p model. While most calculations in the context of ruthenates are based on d-only models (see, e.g., Refs. [7,8,27,28]), there are only few exceptions where the d-p model is used, e.g., in Ref. [29]. There, calculations have been carried out within the Hartree-Fock scheme using estimates for the Hamiltonian parameters. Of course, the d-p model, as opposed to the d-only model, implies a number of additional Coulomb parameters such as U_{pd} and U_{pp}, knowledge of which is poor, as also mentioned explicitly, e.g., in Ref. [29]. First-principles (cRPA) calculations of U_{pd}, U_{pp} are not even implemented in the packages that we have access to. Linear response DFPT, though, can in principle calculate these values but the accuracy of such values is questionable (see calculations reported in Ref. [30]). Furthermore, the inclusion of U_{pd} naturally leads to

a Hamiltonian with nonlocal interactions, which is beyond the applicability of single-site DMFT. Hence, a different, much more expensive approach such as cluster extensions of DMFT would be needed. An additional complexity when using a d-p model is the issue of the double-counting correction, as discussed, for instance, by Hansmann *et al.* [31]. Considering the uncertainties and difficulties of handling the d-p model within the *ab initio* scheme of DFT + DMFT, we thus refrain from carrying out calculations in the d-p model and instead choose the effective low-energy d-only model (the t_{2g} model, in particular).

We emphasize, though, that the hybridization with O p is taken into account by considering a downfolded t_{2g} orbital basis, in which O p degrees of freedom are not thrown away, but included in the tail of the t_{2g} Wannier functions.

The e_g and t_{2g} orbitals are defined in the Ru-O octahedra-based local coordinate system, with the z axis pointing along one of the Ru-O bonds, and the y axis pointing approximately to the neighboring Ru-O band. In $4H$ phase due to the presence of trigonal distortion in the RuO_6 octahedra, the t_{2g} orbitals defined in this oxygen-based coordinate system, are not degenerate, rather they are split into singly degenerate a_{1g} and doubly degenerate e_g^π formed by suitable linear combination of t_{2g} orbitals, with the z axis pointing along the threefold $C3$ axis. WANNIER90 projects to a local coordinate system, and hence any projections with spherical harmonics correctly identify the orbitals in their projections.

The Anderson impurity problems were solved using the continuous-time quantum Monte Carlo algorithm in the hybridization expansion (CT-HYB) [32] as implemented in the TRIQS/CTHYB package [33]. We used the density-density variant of the Kanamori interaction [34]. For our calculations we not only use the cRPA values but also U values ranging from 1 to 4 eV and J values ranging from 0.1 to 0.5 eV to explore the phase diagram. We have set the intraorbital interaction to be $U' = U - 2J$. Real-frequency results have been obtained using the maximum-entropy method of analytic continuation as implemented in the TRIQS/MAXENT application [35]. It is to be noted here that there might be an effect of electronic correlations on the optimization of the crystal structure, which is not captured in one-shot DMFT calculations. However, the focus of the present study is not to optimize the lattice within one structure, but to compare two very different structures, $3C$ and $4H$. Therefore, even if correlation effects would lead to slightly different optimized atomic positions in $4H$ (although unlikely since DFT and experiments fit nicely in that respect), it does not affect the qualitative changes between $3C$ and $4H$ (corner shared vs face shared).

As quantum Monte Carlo solvers are limited to higher temperatures, we also employed an impurity solver based on matrix product states in a special geometry, the fork-tensor-product-states (FTPS) solver [36]. This allows efficient $T = 0$ calculations for multiorbital systems directly on the real-frequency axis. To do so, we discretized the hybridization function using 50 bath sites per spin, and calculated the ground state using a density-matrix-renormalization group algorithm. The time evolution for calculating the interacting Green's functions was done using the time-dependent varia-
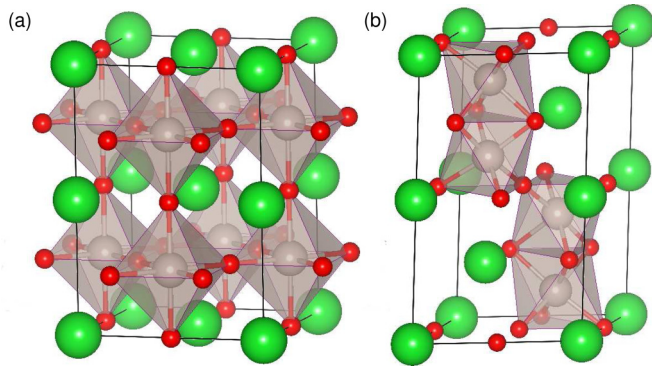
FIG. 1. Structures of the (a) cubic 3*C* and (b) hexagonal 4*H* phase of BRO. The cubic phase is a perovskite structure with all corner-sharing RuO$_6$ octahedra, while the 4*H* hexagonal phase consists of face-shared dimers of RuO$_6$ octahedra, corner-sharing with each other. The green spheres represent Ba, red spheres represent O, and mauve spheres represent Ru.

tional principle using 100 time steps of length $dt = 0.1$ [37]. The calculations were checked for consistency with the full Kanamori Hamiltonian for the 3*C* structure.

III. CRYSTAL STRUCTURE AND DFT BAND STRUCTURE

In Fig. 1 we show the crystal structure of both the 3*C* and the 4*H* phase. As already mentioned, depending on the synthesis condition, the stacking of BaO$_3$ layers can be of the hexagonal close-packed stacking (*h*) or the cubic close-packed stacking (*c*). These two different stacking patterns give rise to face-shared and corner-shared connectivity of neighboring RuO$_6$ octahedra in 4*H* and 3*C* phases, respectively.

The 3*C* structure has a perfect cubic symmetry $Pm\bar{3}m$, and has lattice constants of $a = b = c = 4.075$ Å, and unit cell $\alpha = \beta = \gamma = 90°$ [10]. The RuO$_6$ octahedra are all corner sharing, with the corner-shared Ru-O-Ru angle of 180°, as in perfect cubic symmetry.

The 4*H* structure has a hexagonal symmetry $P6_3/mmc$, and has lattice constants of $a = b = 5.729$ Å and $c = 9.5$ Å, and unit cell angles $\alpha = \beta = 90°$ and $\gamma = 120°$, as given by hexagonal symmetry. The RuO$_6$ octahedra form face-shared dimers, and the dimers are corner-shared between themselves, giving rise to a *hchc* stacking sequence, which indicates a stacking of alternate hexagonal and cubic units. The face-shared dimers have an internal Ru-O-Ru angle of 78.5°, while the corner-shared dimers have a Ru-O-Ru angle of 180° [38]. The percentage of corner-shared connectivity is 100% and 50% for the 3*C* and 4*H* phases, respectively. This difference in connectivity plays a big role in the properties of the two phases as we shall see in a later section.

In Figs. 2(a) and 2(b), we present the DFT band structure and density of states (DOS) obtained from nonmagnetic plane-wave calculations using VASP of 3*C* and 4*H* phases. There are 20 Ru bands for 4 Ru atoms (5 *d* orbitals each) in the unit cell of both 3*C* and 4*H* phases. The states are projected to Ru *d* (red symbols and lines in Fig. 2) and O *p* orbital degrees of freedom (green symbols and lines in Fig. 2). Within
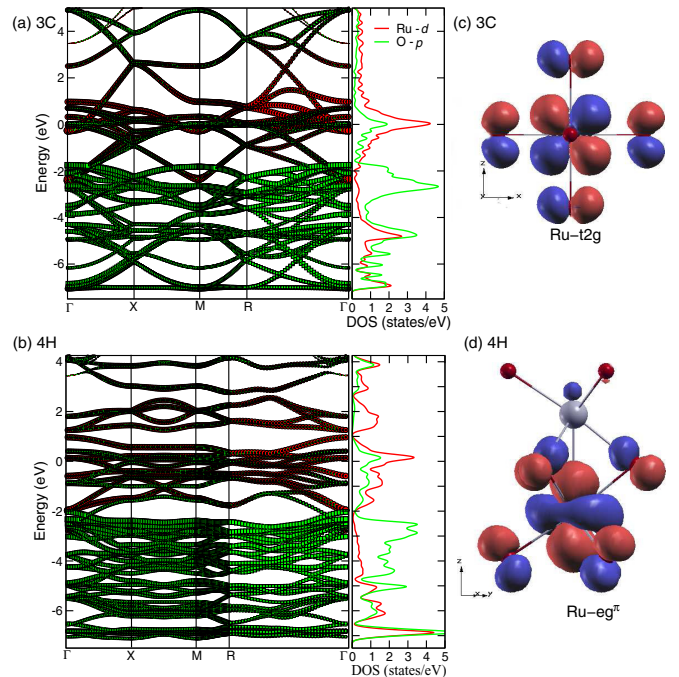

FIG. 2. Nonmagnetic DFT band structure of the (a) cubic 3*C* and (b) hexagonal 4*H* phase of BRO, projected to Ru *d* and O *p* states. (c) and (d) shows the one of the three t_{2g} Wannier orbitals for 3*C* and 4*H* structures, respectively, plotted at an isosurface value of 0.015. The gray spheres represent Ru centers and maroon spheres represent O centers. The lobes of Wannier function isosurfaces, shown in red and blue, represent positive and negative signs of the function, respectively.

the non-spin-polarized scheme of calculations, both systems are metallic with Ru t_{2g} states crossing the Fermi level, with a strong admixture of O *p* states. The computed electronic structure is in good agreement with what has been reported earlier [39]. Comparing the DFT electronic structure of 3*C* and 4*H* we observe a marked difference, in terms of the Ru *d* band width as well as the charge-transfer energy between Ru *d* and O *p* states, which we infer from the band centers of Ru *d* and O *p* bands. The latter is expected to be important in the calculation of the screening of Coulomb parameters *U* and *J*. We further notice multiple peaks in the DOS of 4*H* compared to that of 3*C*, which arises due to bonding-antibonding splitting of trigonally split Ru t_{2g} states as discussed in Ref. [39]. It has also been seen in previous calculations that there is an energy gap of approximately 3 eV between the t_{2g} levels around Fermi energy and the e_g levels at higher energies [39]. Moreover, Wannier projections to both the t_{2g} subspace as well as to the full *d* manifold yields an occupation of four electrons. Hence, only the t_{2g} levels are relevant in our case and are considered in the subsequent DMFT study of the low-spin state of Ru. In Figs. 2(c) and 2(d), the representative low-energy Wannier functions of 3*C* and 4*H* are shown, with lobes of opposite signs of wave functions colored as red and blue. The head part of the Wannier functions situated at Ru sites are shaped according to the *xz* symmetry for 3*C* and e_g^π symmetry for 4*H*, while the tails are shaped in downfolded O *p* symmetry. The maximum spread of the Wannier functions

for 3C is found to be 2.774 Å^2, while that for 4H is 5.067 Å^2. This analysis already points to the higher hybridization of Ru d and O p in 4H than in 3C.

IV. DEGREE OF CORRELATION AND POSSIBLE MAGNETIC ORDERING PATTERNS

To take into account the correlation effect of Ru 4d states, we first carry out single-impurity DMFT calculations for a Ru t_{2g}-based low-energy Hamiltonian defined in the basis of DFT-derived Wannier functions. In particular, we solve the impurity problem only for one Ru atom and use the resulting self-energy on all of the four Ru atoms. A local Coulomb interaction of density-density type between the orbitals is introduced. The interaction part of the Hamiltonian is given b,

$$H_{ii}^{int} = \sum_{i,m=1}^{3} U n_{i,m\uparrow} n_{i,m\downarrow}$$
$$+ \sum_{i,m\neq m'} \sum_{\sigma,\sigma'} (V - J\delta_{\sigma,\sigma'}) n_{i,m\sigma} n_{i,m'\sigma'},$$

where i is the lattice site, and m and m' represent orbital indices. U is the Coulomb repulsion between two electrons with opposite spin in the same orbital. Orbital rotational symmetry is imposed by setting $V = U - 2J$, where J is the Hund's coupling, which lowers the energy of a configuration with different orbitals ($m \neq m'$), and parallel spins $\sigma = \sigma'$. In this section, the effective impurity problem is solved within DMFT by using the hybridization expansion continuous-time quantum Monte Carlo which works at finite temperatures. In the following, we vary the value of U within a range of 1–4 eV and J in the range of 0.1–0.5 eV, which are sensible parameter ranges for 4d transition metal oxides [8].

A. Coherence to incoherence crossover

A crossover from a rather coherent correlated metal with small scattering rates to an incoherent metal with large scattering rates with changes of Hund coupling J has been demonstrated for the 3C phase in a previous study [8]. We find the same to be true for the 4H phase, as determined by the single-impurity DMFT self-energy $\Sigma(i\omega_n)$. Figure 3 summarizes the results which shows the imaginary part of Matsubara self-energies of 3C and 4H for fixed $U = 2.3$ eV and inverse temperature $\beta = 40$ eV^{-1}, for a range of J values. For small values of J, the low-frequency limit of the self-energy is small; for $J = 0.1$ eV the extrapolation gives almost vanishing $-\text{Im}\Sigma(i\omega_n \rightarrow 0)$. Upon increasing J, a deviation from such a behavior is found at low ω_n, manifested as the nonzero intercept of $-\text{Im}\Sigma(i\omega_n \rightarrow 0)$. For 3$C$ [Fig. 3(a)], we observe a progressively increasing scattering rate from very small values for $J = 0.1$ eV and also for $J = 0.2$ eV, to large values for larger Hund's couplings. A very similar behavior is observed for 4H]Fig. 3(b)], which confirms the importance of Hund's coupling for strong-correlation effects in both 3C and 4H. This behavior of increasing scattering rates as a function of J, which implies incoherent electronic states at least at elevated temperatures, is well known from other ruthenate compounds [40], as well as other Hund's metals such as iron selenides [41].
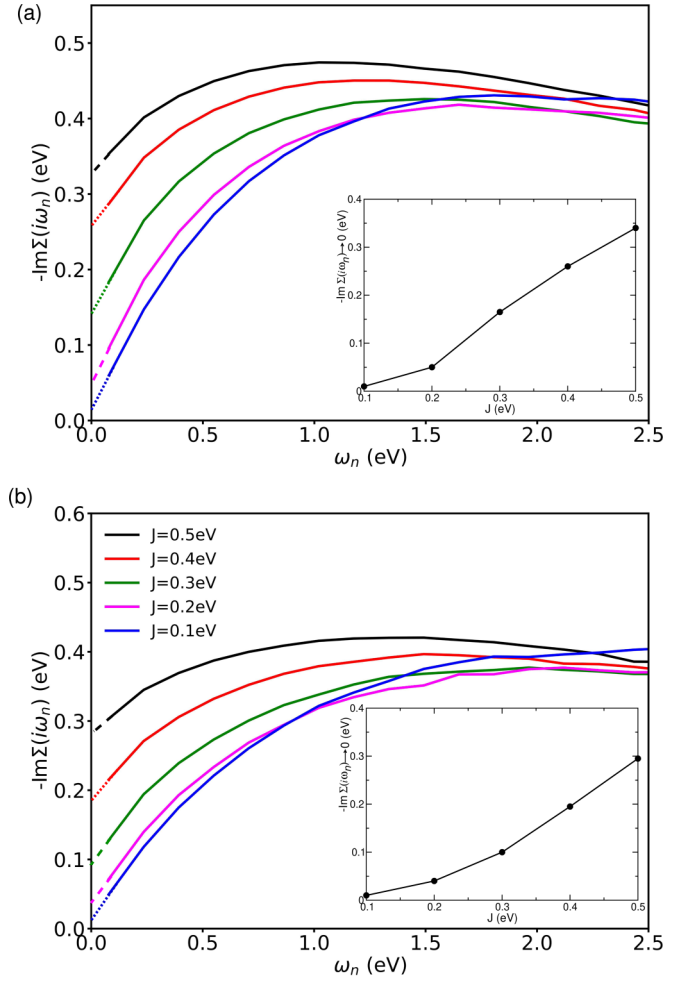

FIG. 3. The imaginary part of self-energies of the (a) cubic 3C and (b) hexagonal 4H phase of BRO, calculated at inverse temperature $\beta = 40$ eV^{-1}. Both phases show a transition from a more coherent behavior with small scattering rates to incoherent behavior with large scattering rates, depending on the choice of Hund J parameter for a fixed $U = 2.3$ eV. The extrapolation of the imaginary part of the self-energies to $\omega_n = 0$ is shown by dotted lines. The inset shows the y-axis intercepts obtained by extrapolation as a function of of J.

B. Correlation-driven magnetism and electronic structure

The paramagnetic correlated spectral function for $U = 2.3$ eV and $J = 0.4$ eV, which are accepted values for ruthenate oxides [40], in 3C and 4H phases at $\beta = 40$ eV^{-1} is shown in Fig. 4. We see that in the paramagnetic phase both structures have metallic ground states. In the case of the 3C cubic state the three t_{2g} orbitals are degenerate, while in the case of 4H the degeneracy between the t_{2g} orbitals is broken, with two degenerate orbitals and another singly degenerate orbital arising due to the trigonal distortion of the RuO$_6$ octahedra in hexagonal symmetry.

Next, we proceed to exploring magnetism within single impurity DMFT by introducing symmetry breaking. For that purpose, we start from the paramagnetic solutions, add a symmetry-breaking term in the form of a spin splitting in the real part of the self-energies, and let the DMFT iterative
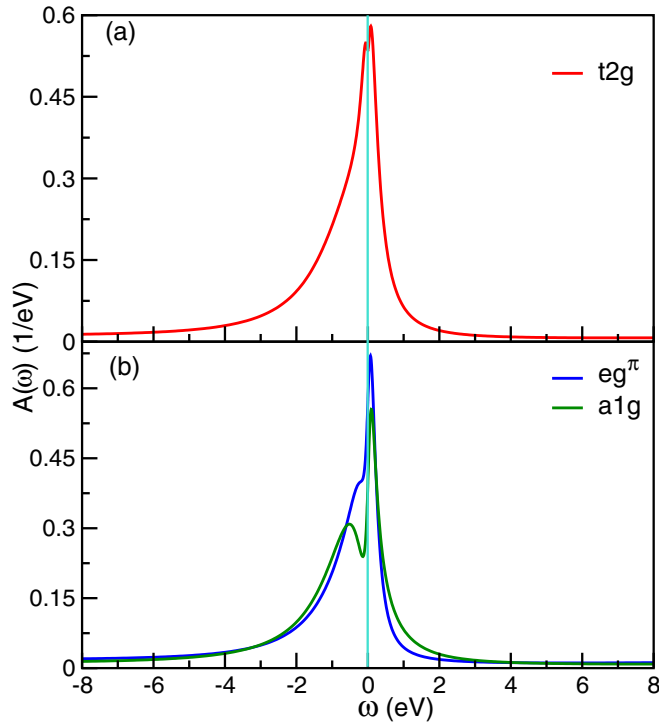
FIG. 4. Correlated spectral functions of the (a) cubic 3C and (b) hexagonal 4H phase of BRO, projected to three t_{2g} states in the paramagnetic phase. The t_{2g} states (red) are degenerate in the 3C phase, while getting split into e_g^π (blue) and a_{1g} (green) states in 4H. The calculations here have been done with $U = 2.3$ eV and $J = 0.4$ eV.

cycle converge to a possible symmetry-broken solution with net ordered magnetic moment. We carry out the calculations at various different values of inverse temperature with β between 40 and 200 eV^{-1}, for both 3C and 4H structures. At $\beta = 40$ eV^{-1}, the calculations are found to converge to a paramagnetic state, while upon reducing temperature, a transition to a magnetic solution is found. In Fig. 5(a), we show a plot of the ordered moments of Ru Wannier functions with the number of DMFT iterations. For the 3C phase we see a stable ferromagnetic (FM) state. A critical temperature of $T_C \approx 116$ K is determined for 3C, albeit the critical temperatures being overestimated [10] due to the mean-field nature of the DMFT calculations. On the other hand, for 4H the ordered moments are found to be not stable, but they rather oscillate as a function of iteration. The reason for these oscillations is that antiferromagnetism naturally gives rise to two distinct sublattices A and B, with the symmetry for the local Green's functions $G_{A,\sigma}(i\omega_n) = G_{B,\bar{\sigma}}(i\omega_n)$. Here, in our ferromagnetic setup, we do not have a sublattice structure, which corresponds to $G_{A,\sigma}(i\omega_n) = G_{B,\sigma}(i\omega_n)$. Since the impurity hybridization function for sublattice A is calculated from the self-energy and Green's function on sublattice B, it is clear that this leads to oscillations, when the sublattice structure and the above given symmetry is not explicitly taken into account.

We next take a look at the spectral functions for the spin-polarized DMFT calculations for the 3C structure, as shown in Fig. 5(b), calculated at $\beta = 100$ eV^{-1}, for $U = 2.3$ eV and $J = 0.4$ eV. We find that in the case of 3C, a
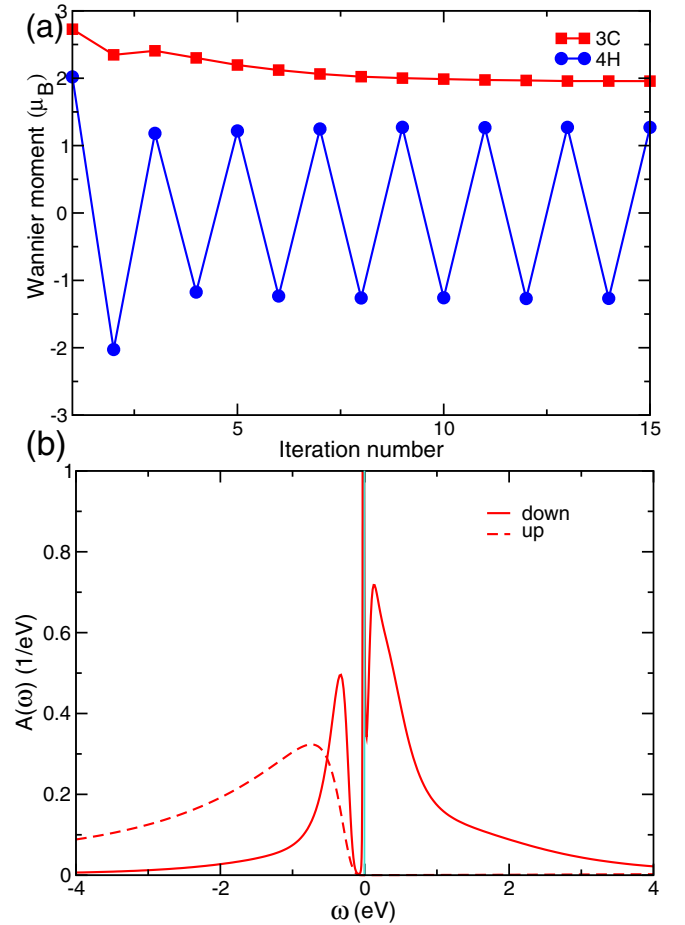

FIG. 5. (a) Variation of Wannier moments as a function of DMFT iterations for both 3C and 4H, showing stable FM moments for 3C and fluctuating moments for 4H. (b) Spectral function of the cubic 3C phase of BRO in the spin-polarized phase. The dashed curve represents the up-spin channel and the solid curve the down-spin channel.

ferromagnetic correlated metallic state appears with the up spin channel majorly occupied and the down spin channel majorly unoccupied. This is in agreement with the experimental observation [10].

C. Variation of interaction parameters and influence on the magnetic phases

Having established the importance of correlations in the description of properties of both 3C and 4H, we next explore the effect of variation of the correlation strength, parametrized through parameters U and J, on the magnetic properties of 3C and 4H. We carry out this exercise primarily due to two reasons. Although we will later in this section estimate the values of U and J from first principles, it is well known that this estimate carries some degree of uncertainty [42]. Second, it has been shown previously that it is possible to tune the Hubbard U and Hund J parameters by application of strain [43]. We thus wish to study the trend of magnetism as a function of U and J values, highlighting the different trends in
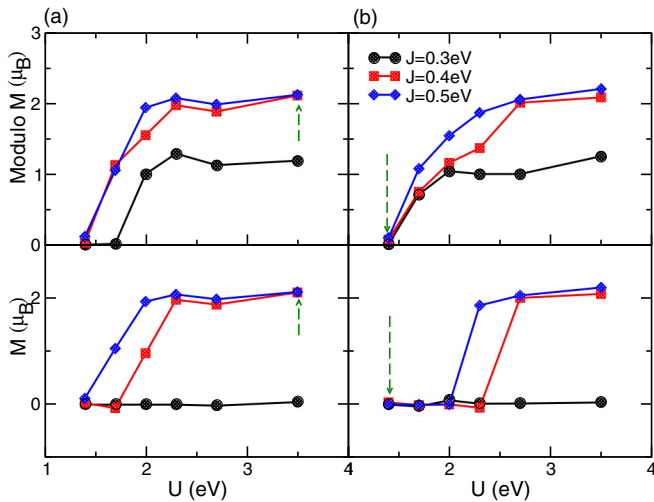
FIG. 6. Variation of magnetic states for (a) cubic $3C$ and (b) hexagonal $4H$ phase with changes of U and J. Modulo M indicates the average value of absolute value of the magnetization over the last four iterations, and M indicates the average magnetization over the last four iterations including its sign. The dashed green arrows in each case mark the cRPA values of U and J.

$3C$ and $4H$, before we proceed to use first-principle estimates to place the actual materials in the phase diagram.

For this purpose, we repeat the symmetry-broken DMFT calculations at $\beta = 100$ eV^{-1}, for a range of U and J values, and monitor two quantities, modulo M and M. The latter refers to the ordered magnetic moment given by $n_{up}-n_{dn}$, n_{up}/n_{dn} being the occupancy in majority and minority spin channels while modulo M refers to the absolute value of the ordered magnetic moment, averaged over the last four iterations of the DMFT cycle. A comparison of these two quantities helps in distinguishing different magnetic states. If there is no magnetic ordering, i.e., the system is in the paramagnetic state, both M and modulo M are zero. If modulo M is finite, but M is zero, antiferromagnetic correlations are signaled. On the other hand, if M is equal to modulo M, a ferromagnetic state is stabilized. We want to stress here that the case when the Wannier moment changes sign over the DMFT iterations, corresponding to $M = 0$ but modulo M finite, is *not* a converged self-consistent DMFT solution. In that sense, this case is not a physically relevant solution. Nevertheless, this behavior signals the tendency to a stable antiferromagnetic (AFM) solution, as the rigorous calculation with an extended unit cell allowing one to host the AFM pattern shows. We will discuss the extended unit cell calculations in the next section.

The variation of modulo M and M within a wide range of values of U and J is shown in Fig. 6. A nontrivial variation of magnetic states is found to be achieved with variation of U and J. One can identify three regions in this phase diagram in general. At small values of U and J one finds a paramagnetic state. With increasing U but still small J, a region is found with moments fluctuating over iterations. With larger values of U and J, a state with stable FM moments is seen.

While this general feature is found to be true for both $3C$ and $4H$, there are subtle differences. For a fixed U value

of 2.3 eV, $3C$ shows moments fluctuating over iterations for $J = 0.3$ eV, and stable FM moments for $J = 0.4$–0.5 eV. The $4H$ phase, however, shows moments fluctuating over iterations for $J = 0.3$–0.4 eV, and stable FM moments only for $J = 0.5$ eV. Fixing now $J = 0.4$ eV, upon variation of U, for the $3C$ structure a fluctuating moment state is found for $U = 1.7$ eV, while a FM state stabilizes beyond $U = 2.3$ eV. We notice that for a large enough U value a fully polarized magnetic moment of $2\mu_B$/Ru is obtained. A previous GGA + U work [39] reported a total moment of $1.2\mu_B$ in $3C$ phase, but for a rather small value of $U = 2$ eV. An experimental work [10] reported the saturation moment to be much less than $2\mu_B$/Ru, though the effective magnetic moment calculated from the paramagnetic phase was found to be close to the saturated value of $S = 1$ for the Ru^{4+} ion. To the best of our knowledge, there does not exist any photoemission experiment on the possible half-metallic nature of cubic FM BaRuO$_3$ as would be the case for fully polarized moments. This calls for further studies.

On the other hand, the $4H$ phase for the same $J = 0.4$ eV shows fluctuating moments until $U = 2.3$ eV, and stabilization of the FM state only beyond $U = 2.7$ eV. This exercise conclusively demonstrates that the magnetic state is crucially dependent on the choice of U and J, with critical U and J values for the stabilization of the FM state as compared to moments fluctuating over iterations being different between $3C$ and $4H$.

The above exercise calls for the need of a first-principles evaluation of U and J values in $3C$ and $4H$ phases. As discussed above, the change of Ru-O covalency due to differences in the connectivity of RuO$_6$ octahedra between $3C$ and $4H$, is expected to influence the screening and, thus, the value of U and J. In particular, we carry out cRPA calculations as implemented within VASP to calculate the Coulomb matrix elements $U_{ijkl}(\omega = 0)$ for the Ru t_{2g} states of BRO in both $4H$ and $3C$ phases. For $3C$ we obtain from cRPA screened $U = 3.5$ eV and $J = 0.5$ eV, and for $4H$ we obtain screened $U = 1.4$ eV and $J = 0.3$ eV. Even considering the standard errors in the estimation of U and J in the cRPA methods, one can see that there is a significant difference between the interaction values for the two phases. The cRPA estimated U and J values for $3C$ and $4H$ are indicated in Fig. 6 with green dashed arrows. With the choice of cRPA estimates, $3C$ falls in the regime of a stable FM state as expected, while $4H$ falls in the regime of fluctuating moments, with vanishingly small oscillating moments. For $4H$, we further find, as the Hubbard U is progressively decreased at fixed $J = 0.3$ eV, the ordered moment keeps decreasing from $U = 2.3$ to $U = 1.7$ eV, and finally vanishes at $U = 1.4$ eV. Thus, at the limit of the cRPA estimated value of Hubbard U for $4H$, the ordered moment vanishes, indicating a lack of any tendency to magnetic long-range order. It is to be noted to cross-check cRPA results, we have also carried out additional calculations for the determination of the Hubbard parameters using the HP package of QUANTUM ESPRESSO [18,19] which calculates Hubbard U in the linear response method. From linear response calculations, we obtain Hubbard U values of $U = 4.55$ eV for $3C$ and $U = 1.88$ eV for $4H$. Keeping in mind that cRPA and linear response are two very different methods for calculating U, these additional calculations provide a confirmation of the
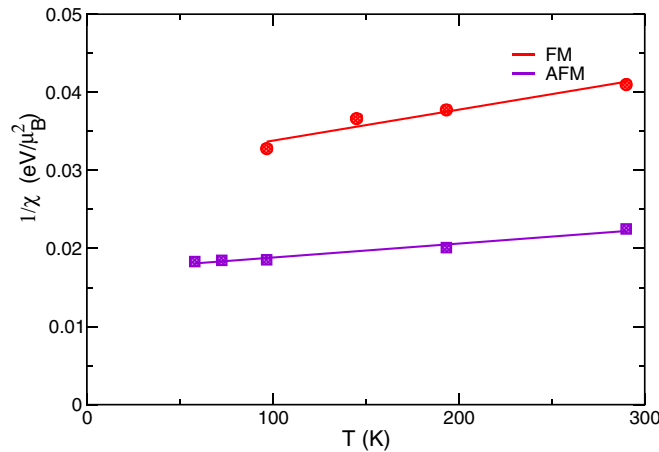
FIG. 7. FM and AFM susceptibility for the 4*H* structure calculated in the supercell with four Ru atoms.

FIG. 8. Wannier moments and density of states of 4H at $T = 0$ K as a function of interaction strength U (with constant $J = 0.3$ eV). The green arrow indicates the cRPA value of $U = 1.4$ eV. It can be seen that a small increase from the cRPA value is sufficient to lead to an (AFM) ordered state.

trend that 3*C* has a much larger interaction parameter as compared to 4*H*. In particular, this provides strong evidence that the U value of 4*H* is small enough to stabilize the FM state. Furthermore, to estimate possible influence of intersite Coulomb repulsion V, we evaluated it in 3*C* phase from the linear response method. The calculated value turned out to be just 0.06 eV, about two orders of magnitude smaller as compared to U.

V. LONG-RANGE ORDER IN 4*H* STRUCTURE

To further elucidate on the nature of magnetism in a 4*H* structure, we expand our DMFT calculation to a multi-impurity problem, in which we treat the four Ru atoms in the unit cell inequivalently, and solve a four-impurity problem with $U = 2$ eV (slightly higher than cRPA estimate), and $J = 0.3$ eV. We carry out calculations at $\beta = 80$–120 eV^{-1}. The four-impurity DMFT calculations at these temperatures result in metallic solutions with vanishingly small ordered moments for 4*H*. However, the small moments show an antifferromagnetic orientation within the Ru-Ru dimer and a ferromagnetic orientation between the dimers. The vanishingly small ordered moment corroborates the experimental finding of absence of long-range magnetic ordering at finite temperatures, with some antiferromagnetic fluctuations [5].

To confirm this further, we carry out susceptibility calculations with both ferromagnetic and antiferromagnetic external magnetic fields (field pointing up on two impurities and pointing down on the other two impurities) on the 4*H* system. We vary the applied field from 0.01 to 0.05 eV in steps of 0.01, and for each value of temperature we obtain the inverse slope of the magnetization vs applied field within the linear regime. This gives the inverse of the uniform susceptibility $1/\chi$ vs temperature T, as shown in Fig. 7. By fitting the curve to a straight line in Fig. 7 we see that the antiferromagnetic susceptibility is much larger than the ferromagnetic susceptibility, thus confirming the possible presence of short-range antiferromagnetic fluctuations in the system.
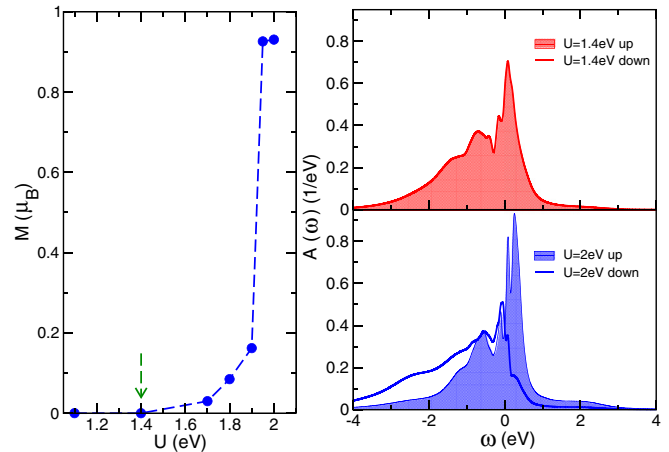
A. Magnetic phase of 4*H* at zero temperature

Having established the absence of long-ranged magnetic ordering of 4*H* at finite temperature that were accessible by quantum Monte Carlo, we next investigate the magnetic phase at $T = 0$ K. We carry out these DMFT calculations using the FTPS solver as implemented in TRIQS. We do spin-polarized calculations with a density-density Hamiltonian, keeping $J = 0.3$ eV fixed and varying U around the cRPA estimated value, from 2 to 1.1 eV.

We find that at the larger values of $U = 2$ and 1.95 eV, the magnetic ordering is stabilized, leading to an antiferromagnetic state with the Ru atoms within the dimer aligned antiferromagnetically, and the dimers themselves being aligned ferromagnetically. It is noteworthy that this is the same antiferromagnetic state that is found in spin-polarized DFT calculations in the same unit cell. However, as the value of U is decreased to 1.9 eV and further down towards the cRPA estimate of 1.4 eV, the ordered moments vanish after a few DMFT iterations. This is shown in Fig. 8. This leads to the conclusion that the magnetic state in 4*H* does not order in experimental studies due to both thermal and quantum fluctuations. The spectral function calculated for $U = 2$ eV and $U = 1.4$ eV is also shown in Fig. 8. As seen, the antiferromagnetic state at $U = 2$ eV, and the nonmagnetic state at $U = 1.4$ eV turn out to be metallic.

VI. CONCLUSION

To conclude, considering the example of 3*C* and 4*H* polytypes of BaRuO$_3$ as a test set, we investigate the effect of geometrical connectivity on magnetic properties of correlated transition metal oxides. The cubic 3*C* and hexagonal 4*H* phases with corner-shared versus face-shared connectivity of RuO$_6$ octahedra are reported to exhibit distinctly different magnetic behavior. While the 3*C* phase shows ferromagnetic ordering with a moderately high magnetic transition temperature of ∼60 K, the 4*H* phase does not order magnetically, but

shows rather paramagnetic behavior with evidence of short-range antiferromagnetic correlation.

The single impurity DMFT calculations for a Ru t_{2g} Hamiltonian shows a crossover from a generalized Fermi liquid to a non-Fermi liquid kind of correlated behavior upon variation of Hund's coupling J in both $3C$ and $4H$ phases, thus characterizing them as correlated Hund's metals. Moreover, we find that the magnetism is highly dependent on the choice of Hubbard U and Hund J coupling, and the trend is not trivial. Depending on the choice of U and J, either an ordered ferromagnetic state, or a paramagnetic state, or a state with ordered moments oscillating over DMFT iterations is achieved for both $3C$ and $4H$. The *ab initio* estimates for the interaction parameters, both from constrained RPA as well as from linear-response calculations, yield significantly larger U and J values for the $3C$ phase as compared to the $4H$ phase. The *ab initio* estimates of U and J place $3C$ in the FM region in the (U, J) parameter space of magnetic phases, while $4H$ is placed in a fluctuating magnetic state but with vanishingly small value of moment. Extending the DMFT calculations to the multi-impurity problem of four Ru atoms in a supercell shows that the magnetic state of $4H$ is indeed paramagnetic with antiferromagnetic short-range fluctuations. This is further confirmed by the uniform ferro- and antiferromagnetic susceptibilities, who show absence of long-range ordering but a larger AFM susceptibility. Finally, the FTPS calculations at $T = 0$ K show that the $4H$ phase is close to a long-range antiferromagnetically ordered metallic state, which can be stabilized upon a slight increase of Hubbard U. This opens up the possibility of exploring exotic antiferromagnetic metallic phases in $4H$ $BaRuO_3$, by strain or a dielectric substrate which is expected to tune the screening, thus influencing the U and J values.

In summary, our study solves the puzzle of the contrasting magnetic behavior of $4H$ and $3C$ polytypes of $BaRuO_3$, and provides a microscopic understanding in terms of the influence of geometric aspects on the magnetic behavior of correlated oxides.

[1] D. I. Khomskii, *Transition Metal Ions in Crystals* (Cambridge University Press, Cmabridge, UK, 2014), pp. 37–93.

[2] A. Georges, L. D. Medici, and J. Mravlje, Annu. Rev. Condens. Matter Phys. **4**, 137 (2013).

[3] Y. Maeno, H. Hashimoto, K. Yoshida, S. Nishizaki, T. Fujita, J. G. Bednorz, and F. Lichtenberg, Nature (London) **372**, 532 (1994).

[4] D. Kan, R. Aso, H. Kurata, and Y. Shimakawa, J. Appl. Phys. **113**, 173912 (2013).

[5] A. Gulino, R. G. Egdell, P. D. Battle, and S. H. Kim, Phys. Rev. B **51**, 6827 (1995).

[6] A. Ali, S. Bansal, B. H. Reddy, and R. S. Singh, *Valence Band Study of $Ba_{1-x}Sr_xRuO_3(x = 0, 0.2)$*, AIP Conf. Proc. No. 2265 (AIP, Melville, NY, 2020), p. 030374.

[7] Q. Han, H. T. Dang, and A. J. Millis, Phys. Rev. B **93**, 155103 (2016).

[8] N. Dasari, S. R. K. C. Sharma Yamijala, M. Jain, T. S. Dasgupta, J. Moreno, M. Jarrell, and N. S. Vidhyadhiraja, Phys. Rev. B **94**, 085143 (2016).

[9] J. G. Zhao, L. X. Yang, Y. Yu, F. Y. Li, R. C. Yu, Z. Fang, L. C. Chen, and C. Q. Jin, J. Solid State Chem. **180**, 2816 (2007).

[10] C.-Q. Jin, J.-S. Zhou, J. B. Goodenough, Q. Q. Liu, J. G. Zhao, L. X. Yang, Y. Yu, R. C. Yu, T. Katsura, A. Shatskiy *et al.*, Proc. Natl. Acad. Sci. USA **105**, 7115 (2008).

[11] C. Felser and R. J. Cava, Phys. Rev. B **61**, 10005 (2000).

[12] P. E. Blöchl, Phys. Rev. B **50**, 17953 (1994).

[13] G. Kresse and J. Hafner, Phys. Rev. B **47**, 558 (1993).

[14] G. Kresse and J. Furthmüller, Phys. Rev. B **54**, 11169 (1996).

[15] P. Blaha, K. Schwarz, F. Tran, R. Laskowski, G. K. H. Madsen, and L. D. Marks, J. Chem. Phys. **152**, 074101 (2020).

[16] J. P. Perdew, K. Burke, and M. Ernzerhof, Phys. Rev. Lett. **77**, 3865 (1996).

[17] G. Pizzi, V. Vitale, R. Arita, S. Blügel, F. Freimuth, G. Géranton, M. Gibertini, D. Gresch, C. Johnson, T. Koretsune *et al.*, J. Phys.: Condens. Matter **32**, 165902 (2020).

[18] I. Timrov, N. Marzari, and M. Cococcioni, Phys. Rev. B **98**, 085127 (2018).

[19] I. Timrov, N. Marzari, and M. Cococcioni, Phys. Rev. B **103**, 045141 (2021).

[20] P. Giannozzi, S. Baroni, N. Bonini, M. Calandra, R. Car, C. Cavazzoni, D. Ceresoli, G. L. Chiarotti, M. Cococcioni, I. Dabo *et al.*, J. Phys.: Condens. Matter **21**, 395502 (2009).

[21] P. Giannozzi, O. Andreussi, T. Brumme, O. Bunau, M. B. Nardelli, M. Calandra, R. Car, C. Cavazzoni, D. Ceresoli, M. Cococcioni *et al.*, J. Phys.: Condens. Matter **29**, 465901 (2017).

[22] J. Kuneš, R. Arita, P. Wissgott, A. Toschi, H. Ikeda, and K. Held, Comput. Phys. Commun. **181**, 1888 (2010).

[23] M. Aichhorn, L. Pourovskii, V. Vildosola, M. Ferrero, O. Parcollet, T. Miyake, A. Georges, and S. Biermann, Phys. Rev. B **80**, 085101 (2009).

[24] M. Aichhorn, L. Pourovskii, and A. Georges, Phys. Rev. B **84**, 054529 (2011).

[25] M. Aichhorn, L. Pourovskii, P. Seth, V. Vildosola, M. Zingl, O. E. Peil, X. Deng, J. Mravlje, G. J. Kraberger, C. Martins *et al.*, Comput. Phys. Commun. **204**, 200 (2016).

[26] O. Parcollet, M. Ferrero, T. Ayral, H. Hafermann, I. Krivenko, L. Messio, and P. Seth, Comput. Phys. Commun. **196**, 398 (2015).

[27] E. Jakobi, S. Kanungo, S. Sarkar, S. Schmitt, and T. Saha-Dasgupta, Phys. Rev. B **83**, 041103(R) (2011).

[28] L. Si, Z. Zhong, J. M. Tomczak, and K. Held, Phys. Rev. B **92**, 041108(R) (2015).

[29] K. Rościszewski and A. M. Oleś, Phys. Rev. B **91**, 155137 (2015).

[30] I. Timrov, GitLab (2018), URL https://gitlab.com/QEF/q-e/-/blob/0c54e893feb35de42695d2d231495d8604224045/HP/examples/example07/reference/LiCoO2.Hubbard_parameters.dat.

[31] P. Hansmann, N. Parragh, A. Toschi, G. Sangiovanni, and K. Held, New J. Phys. **16**, 033009 (2014).

[32] P. Werner and A. J. Millis, Phys. Rev. B **74**, 155107 (2006).

[33] P. Seth, I. Krivenko, M. Ferrero, and O. Parcollet, Comput. Phys. Commun. **200**, 274 (2016).

[34] J. Kanamori, Prog. Theor. Phys. **30**, 275 (1963).

[35] G. J. Kraberger, R. Triebl, M. Zingl, and M. Aichhorn, Phys. Rev. B **96**, 155128 (2017).

[36] D. Bauernfeind, M. Zingl, R. Triebl, M. Aichhorn, and H. G. Evertz, Phys. Rev. X **7**, 031013 (2017).

[37] D. Bauernfeind and M. Aichhorn, SciPost Phys. **8**, 024 (2020).

[38] S.-T. Hong and A. W. Sleight, J. Solid State Chem. **128**, 251 (1997).

[39] S. Kanungo, R. Datta, S. K. Panda, and T. Saha-Dasgupta, J. Phys.: Condens. Matter **25**, 505503 (2013).

[40] J. Mravlje, M. Aichhorn, T. Miyake, K. Haule, G. Kotliar, and A. Georges, Phys. Rev. Lett. **106**, 096401 (2011).

[41] M. Aichhorn, S. Biermann, T. Miyake, A. Georges, and M. Imada, Phys. Rev. B **82**, 064504 (2010).

[42] H. Shinaoka, M. Troyer, and P. Werner, Phys. Rev. B **91**, 245156 (2015).

[43] B. Kim, P. Liu, J. M. Tomczak, and C. Franchini, Phys. Rev. B **98**, 075130 (2018).